Elasticity reconstruction from experimental MR displacement data: initial experience with an overlapping subzone finite element inversion process

E. E. W. Van Houten
Thayer School of Engineering, Dartmouth College, Hanover, New Hampshire 03755

J. B. Weaver
Department of Radiology, Dartmouth Hitchcock Medical Center, Lebanon, New Hampshire 03766

M. I. Miga and F. E. Kennedy
Thayer School of Engineering, Dartmouth College, Hanover, New Hampshire 03755

K. D. Paulsen
Thayer School of Engineering, Dartmouth College, Hanover, New Hampshire 03755, and Norris Cotton Cancer Center, Lebanon, New Hampshire 03766

(Received 6 May 1999; accepted for publication 22 October 1999)

The determination of the elastic property distribution in heterogeneous gel samples with a finite element based reconstruction scheme is considered. The algorithm operates on small overlapping subzones of the total field to allow for a high degree of spatial discretization while maintaining computational tractability. By including a Maxwellian-type viscoelastic property in the model physics and optimizing the spatial distribution of this property in the same manner as elasticity, a Young's modulus image is obtained which reasonably reflects the true distribution within the gel. However, the image lacks the clarity and accuracy expected based on simulation experience. Preliminary investigations suggest that transient effects in the data are the cause of a significant mismatch between the inversion model, which assumes steady-state conditions, and the actual displacements as measured by a phase contrast MR technique. © *2000 American Association of Physicists in Medicine*.[S0094-2405(00)01901-5]

Key words: MR elastography, experimental elasticity reconstruction, viscoelastic tissue behavior, finite element inversion techniques

I. INTRODUCTION

Interest in accurate, quantitative evaluation of the physical properties of biological tissue is rapidly increasing as the value of this information has been appreciated in such applications as lesion detection, medical examination, and computer assisted surgical procedures. One particular area of interest includes the assessment of the elastic properties of tissue through the analysis of noninvasive image-based, strain measurements. Ultrasound elastography has been studied for some time,[1–8] where ultrasonic imaging is used to detect subsurface displacement response to an externally applied displacement source. While ultrasound elastography continues to hold promise in terms of providing valuable tissue data, it is presently limited by the lack of lateral resolution in ultrasonic imaging compared to other available modalities. This potential drawback has led to the investigation of MR-based strain imaging techniques.[9–14] In addition to fully three-dimensional imaging capabilities, MR offers higher resolution than ultrasound, making it a very appealing method for discerning micron level displacement fields in biological structures.

Regardless of the strain imaging technique, it is generally agreed that some type of model-based reconstruction procedure is required for determination of elastic property distributions.[15,16] To date these models have varied widely in complexity, from simple algorithms relating a Local Frequency Estimation (LFE) to stiffness via a standard wave equation formulation[17] to nonlinear inversion schemes which operate on a partial differential equation (PDE).[3,18–22] While many of the methods proposed to date have shown promise in simulation, there has been limited success in producing accurate inversions of measured dynamic strain data. This points to a variety of issues, such as viscoelastic behavior and transient effects, which need investigation in order to develop successful, robust algorithms for elasticity imaging through interpretation of harmonic displacement fields.

While inversion in the case of dynamic, rather than quasi-static, mechanical motion has shown the need for a high level of algorithmic sophistication, the benefits of the procedure are potentially significant. By generating strain fields through dynamic displacement propagation, elasticity information can be inferred in structures inaccessible by means of quasi-static surface actuation, e.g., the brain. In addition, dynamic displacements are useful for estimating tissue properties other than elasticity, such as dispersion and density. This paper examines the first applications of a subzone-based elastic property reconstruction scheme,[20] with an additional Maxwellian-type viscoelastic term, to experimental MR data. This algorithm is based on a well-established nonlinear inversion scheme,[3,18,19] where the global reconstruction technique is instead performed on small, local ''subzones'' of the tissue region of interest (ROI). The improvements in algo-

rithmic performance found through the addition of viscoelastic behavior are encouraging but not complete. Evidence presented here suggests that the method's assumption of steady-state motion in the MR generated data may be the primary discrepancy in the data-model match.

II. INVERSION METHOD

The nonlinear elastic property reconstruction scheme that forms the core of the subzone inversion technique is centered around a squared error minimization formulation,[3,18–20] where the agreement between the calculated displacements derived from the most recent property estimate, $\mathbf{u}_l^c$ at location l, and the measured displacement data at that location, $\mathbf{u}_l^m$, is sensed by the functional

$$\mathbf{F}=\sum_{l=1}^{N}(\mathbf{u}_l^m-\mathbf{u}_l^c)^2, \tag{1}$$

for N measurement locations. Minimization of this functional is accomplished by equating its derivatives with respect to the reconstruction parameters to zero, generating the matrix system

$$[(\mathbf{H}+\alpha\mathbf{I})]\{\Delta\boldsymbol{\Gamma}\}-\{\mathbf{f}\}=\mathbf{0}, \tag{2}$$

with $\Delta\boldsymbol{\Gamma}$ representing the vector of parameter updates, $\mathbf{f}$ being the derivatives of $\mathbf{F}$ in Eq. (1) with respect to the parameter field $\boldsymbol{\Gamma}$, and $\mathbf{H}$ being the approximate Hessian matrix. The regularization parameter α is added to the diagonal of $\mathbf{H}$ and scaled to the inversion problem at hand by the Levenberg–Marquardt method[23] to facilitate solution of Eq. (2).

Two elastodynamic models have been implemented to date in order to provide displacement calculations based on the estimated parameter distributions. The simplest involves an undamped linear elastic relationship, while the other adds a Maxwellian viscoelastic coefficient to account for the attenuation of displacement in tissue. Expressed in terms of a PDE in displacement, $\mathbf{u}$, these models can be written as[24]

$$\nabla\cdot G\nabla\mathbf{u}+\nabla(\lambda+G)\nabla\cdot\mathbf{u}=\rho\frac{\partial^2\mathbf{u}}{\partial t^2}, \tag{3}$$

for a linear elastic tissue of density ρ having properties G and λ and

$$\nabla\cdot G\nabla\mathbf{u}+\nabla(\lambda+G)\nabla\cdot\mathbf{u}=\zeta\frac{\partial\mathbf{u}}{\partial t}+\rho\frac{\partial^2\mathbf{u}}{\partial t^2}, \tag{4}$$

for a Maxwellian viscoelastic material with damping coefficient ζ.

In general, the inversion problem defined in Eq. (2) is intractable for highly resolved material property distributions as computing a single solution update scales cubically with the size of the vector $\boldsymbol{\Gamma}$. To overcome this resolution limitation, a subzone inversion scheme has been developed[20] which recasts the global error functional in Eq. (1) as a sum of functionals defined on small subzones of the total ROI,

$$\mathbf{F}=\sum_{z=1}^{Q}\mathbf{F}_z \tag{5}$$

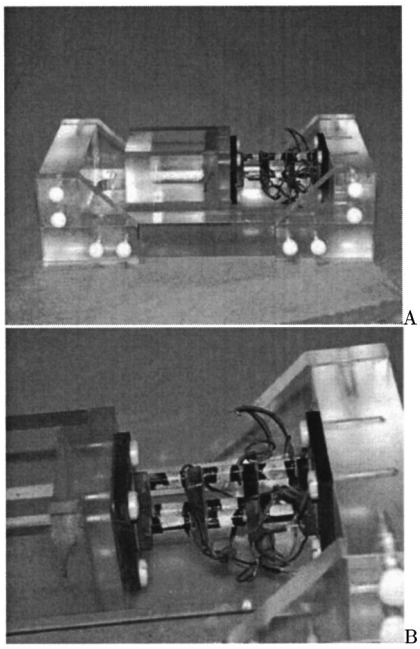

FIG. 1. Piezoelectric displacement actuator with image A showing the entire device including the phantom box on the left and image B showing a close up of the nine parallel driven piezocrystal stacks attached to one wall of the rigid phantom container. The imparted motion is parallel to the long axis of the piezoelectric actuator which is denoted as the x direction in subsequent figures.

where min($\mathbf{F}$) is replaced by

$$\sum_{z=1}^{Q}\min(\mathbf{F}_z) \tag{6}$$

for Q subzones. Further details on the mathematical and computational underpinnings of this technique are described in Ref. 20; the algorithm essentially relying on foundations previously developed in Refs. 18, 19. In numerical simulations the formulation has been found to be very effective in reconstructing high resolution (MR pixel level) parameter distributions even in the presence of high noise (up to 15% in the undamped linear elastic case), as reported in Ref. 20. The subzone-based inversion method has also been found to execute relatively quickly, with global property distribution solutions for meshes of approximately 20 000 nodes being completed in a few hours. Direct solution of the full inverse problem for a mesh of this size is computationally infeasible on workstations currently available. Here, we describe our initial experience in applying the algorithm to dynamic MR displacement data measured in gel phantoms.

III. MR DISPLACEMENT IMAGING TECHNIQUE

To obtain displacement measurements, we have developed an MR-compatible mechanical driver which can vibrate tissue-like gel phantoms in a strong magnetic field. Figure 1 shows the device which is currently in use. The design is centered around an actuator constructed of nine piezoelectric stacks wired in parallel. Three layers, each separated by stabilizing ceramic plates and consisting of three piezostacks,

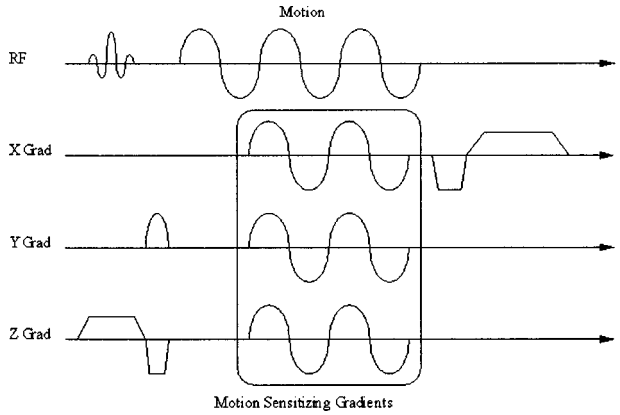

FIG. 2. MR motion sensitizing gradient sequence showing that the duration of mechanical motion is directly linked to the data acquisition time associated with one phase encoding event.

were used to provide adequate displacement under dynamic load. Individually, each stack is capable of ± 7 μm of displacement when driven by a 100-Vpp signal, so that the assembly as a whole can ideally produce ± 21 μm of motion. The stacks are powered by a wide band amplifier which boosts the sinusoidal driving signal generated by the MR pulse program. Using the MR pulse sequence to generate the driving signal for mechanical vibration allows almost any waveform to be used and also allows highly accurate control of the phase between the mechanical vibration and the motion encoding gradient. However, this also limits the time of mechanical stimulation to the signal duration of the motion sensitizing gradients as described below (see Fig. 2). Independent measurements of actuator motion using a capacitively coupled displacement probe have demonstrated that the response of the actuators is linear in the applied voltage for a given frequency, yielding 10–15 μm of displacement at 100 Hz, 60 Vpp.

The motion encoding MR gradient sequence, based on a simple gradient echo sequence, is illustrated in Fig. 2. The imaging process involves three cycles of mechanical motion driven by signal from the RF, the last two of which coincide with the sensitizing gradients. The phase in the MR image is recorded for different phase relationships between the applied motion and the encoding gradients to calculate the harmonic displacement in each pixel of an image. Four such phase relationships are used to ensure internal consistency between the measured phase and the fit to the expression $C + M\cos\varphi$, where the amplitude, M, and the relative phase, φ, completely characterize the harmonic motion. The constant phase offset, C, has no bearing on the measured motion. MR timing and resolution parameters for these image acquisitions are: $TR = 300$ ms; $TE = 58$ ms; $FOV = 8$ cm; 256×128 pixels; 10-mm slice thickness.

IV. EXPERIMENTAL RESULTS

Initially, homogeneous gels were used to validate the MR measurement system. Figure 3 shows a typical example of the displacements obtained in a homogeneous gel phantom ($5\text{ cm} \times 5\text{ cm} \times 4\text{ cm}$), where the 100-Hz, x-directed actuation was applied through the bottom and two side walls of the rigid gel container (see Fig. 1). The displacements were recorded in both the horizontal (x) and vertical (y) directions such that they form a two component vector field in the imaging plane parallel to the axis of mechanical translation. Because of the symmetry in this case, only a single central plane is illustrated. Distortional (shear) wave fronts are evident with a wavelength of approximately 1 cm. This wavelength is consistent with the known Young's modulus of the gel (3–5 kPa, as measured in separate mechanical tests). Peak displacements measured in the gel at the walls of the box were approximately 10 μm, which mirrors the data collected with an independent measurement probe.

In Fig. 3, the images in the first column represent data collected for x-directed (horizontal) motion while the second column shows the corresponding data for y-directed (vertical) motion. The first row, A, shows a standard grayscale MR image of the homogeneous gel phantom, while rows B and C show the reconstructed motion parameters M and φ, respectively. The bottom row, D, shows the overall displacement field, given by $M\cos\varphi$ for each vector displacement component. It is interesting to note that there is a small discrepancy between these displacement images and the known boundary conditions, i.e., a nonzero displacement along the bottom of the gel phantom. This is due to an imperfection in an early prototype of the mechanical driver, where the horizontal plane of motion did not exactly correspond to the horizontal plane of the MR, leading to a uniform y-directed displacement offset within the gel.

The development of wavelike behavior is readily visible in the magnitude (row B) and displacement fields (row D) as expected. However, the mechanics of the wave propagation are fairly complex, even for a homogeneous gel phantom as illustrated in Fig. 3, due to the asymmetric (top to bottom) boundary conditions which exist. From the x directional displacement (row D, left), it is evident that the predominant mode of wave propagation is shear motion caused by the bottom surface acting as a distortional wave source. The uniform horizontal peaks and valleys suggest the gel is nearly incompressible at this length scale (short compared to the dilatational wavelength) and low frequency, so that dilatational wave propagation is not supported. The same conclusion is reached by examining the y motion in Fig. 3 (row D, right) where uniform vertical contours exist, indicating a shear mode of propagation. Another noticeable characteristic is the apparent damping of motion from the walls to the center of the gel (row B) suggesting that the wavefronts may have undergone some dispersion or may not represent fully developed harmonic motion.

Figure 4 shows MR generated x and y displacement data for a block of agar gel with a hard, spherical agar gel inclusion approximately 1.5 cm in diameter. The plane shown is the same as Fig. 3, cutting through the center of the phantom with its x-axis in line with the direction of vibration. The y-directed displacement offset associated with Fig. 3 has been removed by the elimination of the imperfection in the mechanical driver. Figure 5 presents a standard grayscale MR image of the gel phantom. Interestingly, the inclusion is

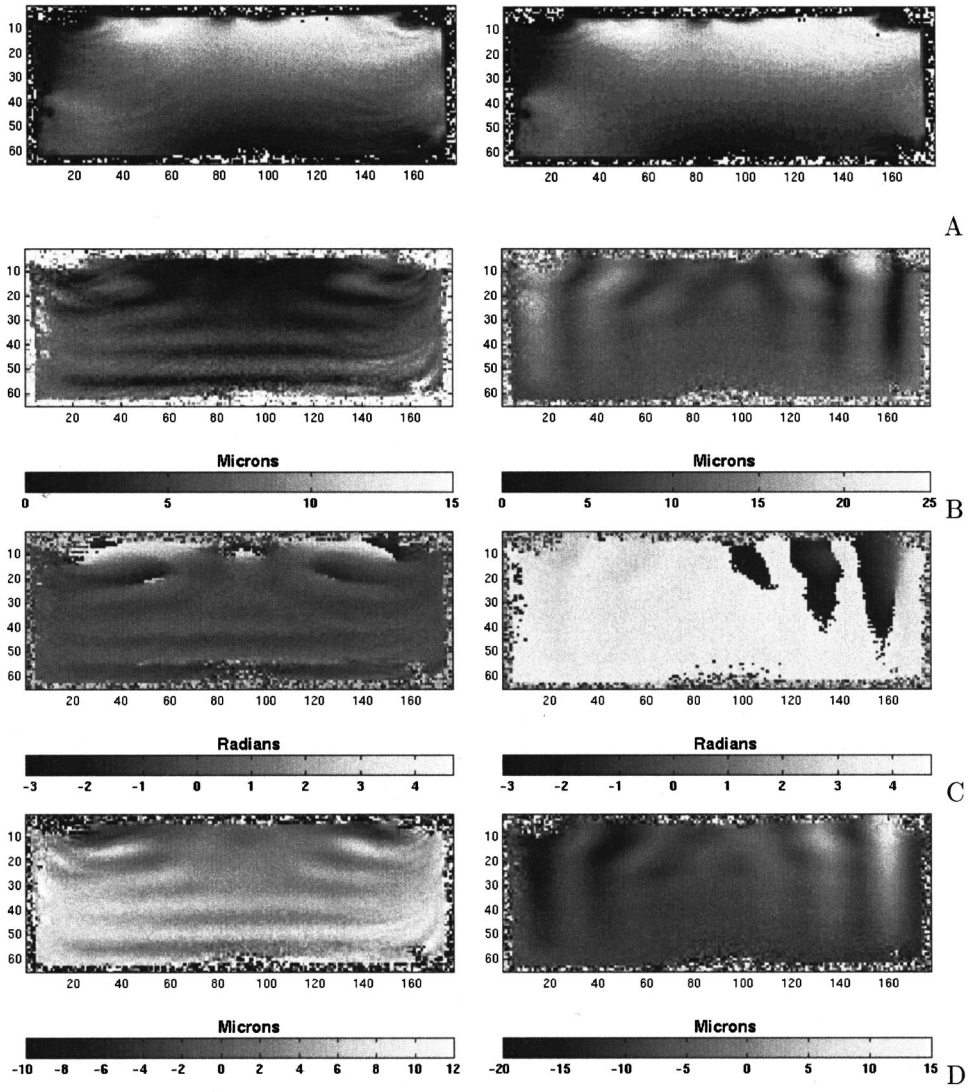

FIG. 3. Raw data from MR motion encoding gradients using a homogeneous gel phantom within the device shown in Fig. 1 with voxel intensity grayscale images (row A), magnitudes of *x* and *y* displacement respectively [μm], (row B), phase of *x* and *y* directional displacement [rad] (row C), and reconstructed *x* and *y* displacement from magnitude and phase [μm] (row D). The left-hand column represents *x* directed motion sensitivity while the right represents *y* directed sensitivity. Note that the images in this figure are dimensioned in pixel coordinates.

barely visible in image A, showing that the elastic property contrast does not translate into conventional MR image contrast. It is also the case that the displacement fields themselves (Fig. 4) do not clearly indicate the presence of the harder inclusion embedded within the gel. For visualization purposes, the area of heterogeneity has been outlined in image B of Fig. 5.

Image reconstructions of the elastic property distribution in the heterogeneous gel sample (Fig. 5) obtained from the MR displacement data (Fig. 4) are presented in Fig. 6. Two inversions are shown: one with the undamped elastic model from Eq. (3) (image A) and the other with the damped model presented in Eq. (4) (images B and C), where image B shows the elasticity distribution and image C shows the map of the Maxwellian attenuation coefficient for the damped model reconstruction. While both images A and B clearly recover the presence of a hard inclusion near the center of the gel, the size and overall localization of the inclusion are more accurately represented in the damped model inversion. Image C indicates that the surrounding gel has a relatively low attenuation component while the inclusion exhibits a level of increased damping.

The results in Fig. 6 are encouraging, especially since they represent one of the first elastic property images derived from experimental MR data where displacements have been measured under conditions of a dynamically applied mechanical stimulus. However, further improvements are desirable and necessary if MR elastography is to progress clinically. While qualitatively satisfying, the images in Fig. 6 are not immediately as promising as those achieved in simulation studies,[20] which raises important questions about the adequacy of the model relative to the imaging physics. The improvement in the elastic property image with the addition of attenuation effects demonstrated in Fig. 6 suggests that data-model match is critical. In this regard it is important to note that the MR displacement field is acquired during the first three harmonic cycles of the displacement stimulation which is intermittently applied with the pulse sequencing (see Fig. 2) as the data associated with each pixel/voxel is generated. Hence, it is quite possible that the measured dis-

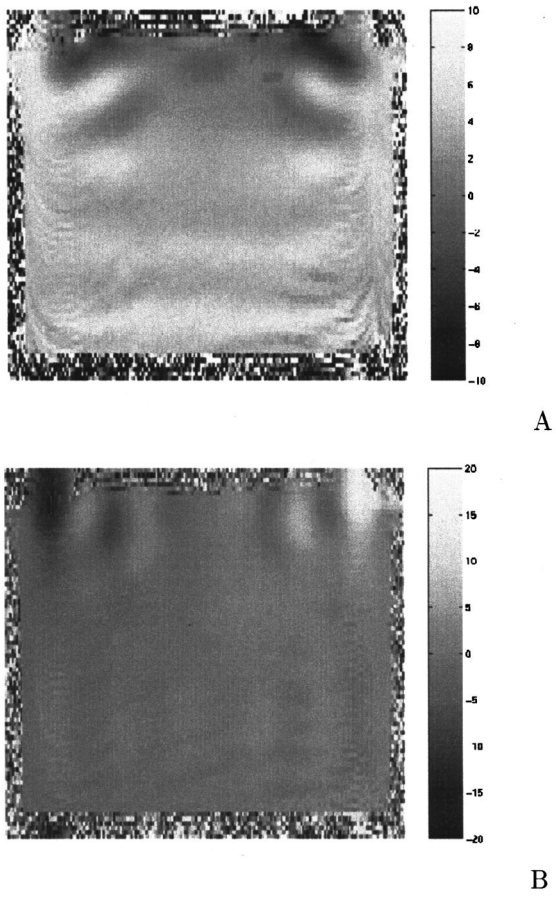

FIG. 4. Displacement data generated by the phase contrast MR imaging method for the gel sample shown in Fig. 5. Image A shows the x direction displacement while image B shows the y direction displacement, both in μm.

placements do not reflect fully developed wavefronts which have reached the dynamic steady state, creating a conflict with the harmonic motion assumption used in the inversion model.

To investigate this possibility, we simulated the transient behavior of the MR data acquisition using a time-domain solution of Eq. (4) where the stimulation was applied to the walls of the phantom for three cycles at 100 Hz. The time history of each node in the finite element mesh which comprises the measured displacement field was then Fourier transformed and the 100-Hz component (magnitude and phase) was extracted in order to represent the MR displacement measurements. This data was then supplied to our frequency domain inversion algorithm (after being corrupted with 10% added noise), which produced the elastic property image shown in image A of Fig. 7. This image is strikingly similar in character to the images in Fig. 6. In image B of Fig. 7, we also show the case where the simulated measurement data is taken from the steady-state solution (with 10% added noise) and inverted with the algorithm. The improvement in the recovery of the elastic property distribution is remarkable and suggests that the degradation of the image in Fig. 6 results in part from data-model mismatch between the transient motion which is measured and the time-harmonic

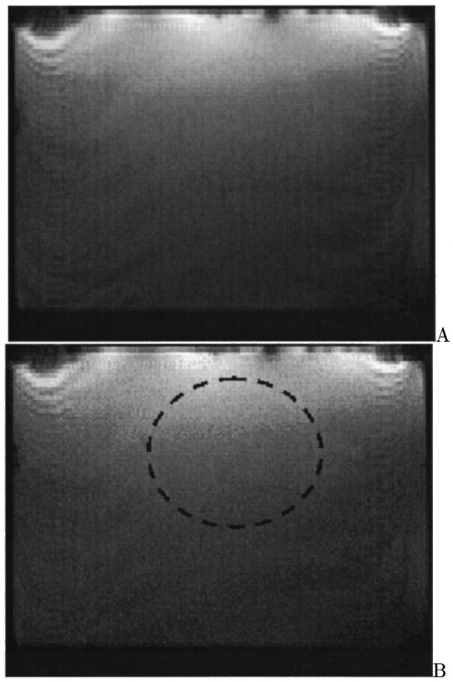

FIG. 5. Standard MR contrast image of a heterogeneous gel sample where image B includes a superimposed outline of the hard inclusion.

model which is assumed. It is also interesting to note that the recovery of the elastic properties is quantitative for the steady-state data image (image B) whereas the reconstructed properties are an order of magnitude too high for the transient data image (image A), presumably due to some form of artificial hardening which tries to compensate for the data-model mismatch. The reconstructions from experimental data in Fig. 6 exhibit the same character (i.e., an effective hardening of the embedded inclusion).

V. CONCLUSIONS

Previous simulations[20] indicate that quantitative image reconstruction of elastic property distributions can be recovered in the presence of considerable measurement noise (up to 15%) using an overlapping zone finite element inversion technique. Reconstructed property resolution can be preserved at the MR measurement level (i.e., pixel resolution) with this approach. Initial experience with reconstructions of actual MR data in heterogeneous gel phantoms consisting of harder inclusions embedded in a softer background is encouraging and shows that the localized increase in stiffness can be found (despite a lack of conventional MR image contrast or contrast observable directly in the displacement field itself). In this regard, the incorporation of displacement attenuation through the addition of a Maxwellian viscoelastic term in the governing computational model has been shown to improve the recovery of the size, shape, and location of the hard inclusion. However, simulations of the potential transient effects in the MR displacement measurements indicate that the data-model mismatch between the MR data acquisition method and the assumed steady-state image recon-

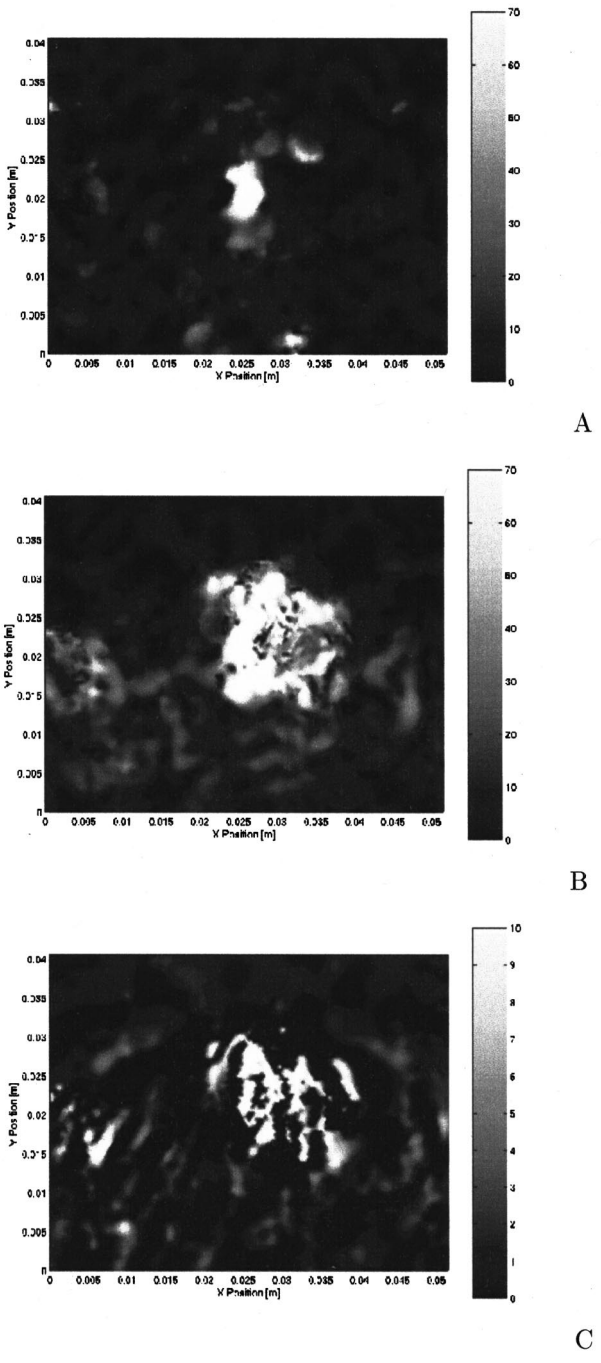

FIG. 6. Two inversions of the MR displacement data shown in Fig. 4. Image A shows the reconstruction based on the undamped linear elastic model in Eq. (3) [kPa] and images B and C show the resulting elasticity (image B) and Maxwellian damping (image C) distributions of the viscoelastic model [Eq. (4)] inversion, in units of [kPa] and [kg/s $1e6$], respectively.

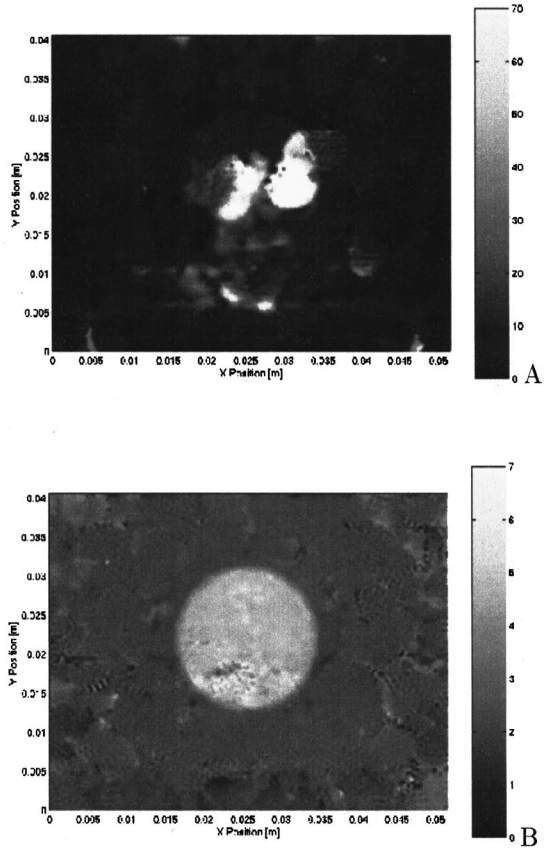

FIG. 7. Two inversions of the simulated data set where image A shows the reconstruction based on displacement data generated in three cycles of motion starting from rest [kPa] while image B shows the same reconstruction process carried out on steady-state data [kPa].

struction model may be the most important factor which presently limits the recovered property image quality.

Two immediate pathways for resolving this inconsistency present themselves. As demonstrated in the transient simulation reported here, the MR displacement encoding gradient imaging process can be modeled by taking the frequency component of the transient displacement solution related to the harmonic excitation. By incorporating this process into the subzone inversion technique, the transient effects present in displacement images generated in three or four cycles of actuation could be modeled, presumably leading to high quality inversions from transient data sets of this type. Alternatively, by separating the driving signal for the mechanical actuator from the gradient signal, but maintaining phase coherency with the MR gradients through the use of a phase-lock loop, mechanical excitation could be applied throughout the image acquisition process. This would assure that the resulting displacement images represent the steady-state motion of the sample, which should also lead to high quality property reconstructions. Which approach provides the best image reconstructions while still offering a convenient and feasible imaging process remains to be determined. At this point both of the strategies mentioned here remain as viable options.

ACKNOWLEDGMENTS

This work was supported in part by NIH Grant No. R01-NS33900, awarded by the National Institute of Neurological Disorders and Stroke and in part by DOD-AMRD, DAMP 17-96-1-6119.

[1] I. Céspedes, J. Ophir, H. Ponnekanti, and N. Maklad, ''Elastography: Elasticity imaging using ultrasound with application to muscle and breast *In Vivo*,'' Ultrason. Imaging **15**, 73–88 (1993).
[2] L. Gao, K. J. Parker, S. K. Alam, and R. M. Lerner, ''Sonoelasticity imaging: Theory and experimental verification,'' J. Acoust. Soc. Am. **97**, 3875–3886 (1995).
[3] F. Kallel and J. Ophir, ''A least-squares strain estimator for elastography,'' Ultrason. Imaging **19**, 195–208 (1997).
[4] R. M. Lerner, S. R. Huang, and K. J. Parker, '' 'Sonoelasticity' images derived from ultrasound signals in mechanically vibrated tissues,'' Ultrasound Med. Biol. **16**, 231–239 (1990).
[5] D. Nicholas, D. K. Nassiri, P. Garbutt, and C. R. Hill, ''Tissue characterization from ultrasound B-scan data,'' Ultrasound Med. Biol. **12**, 135–143 (1986).
[6] J. Ophir, I. Céspedes, H. Ponneckanti, Y. Yazdi, and X. Li, ''Elastography: A quantitative method for imaging the elasticity of biological tissues,'' Ultrason. Imaging **13**, 111–134 (1991).
[7] Y. Yamakoshi, J. Sato, and T. Sato, ''Ultrasonic imaging of internal vibration of soft tissue under forced vibration,'' IEEE Trans. Ultrason. Ferroelectr. Freq. Control **37**, 45–53 (1990).
[8] A. R. Skovoroda, S. Y. Emelianov, M. A. Lubinski, A. P. Sarvazyan, and M. O'Donnell, ''Theoretical analysis and verification of ultrasound displacement and strain imaging,'' IEEE Trans. Ultrason. Ferroelectr. Freq. Control **41**, 302–313 (1994).
[9] J. Bishop, G. Poole, M. Leitch, and D. B. Plewes, ''Magnetic resonance imaging of shear wave propagation in excised tissue,'' J. Magn. Reson. Imaging **8**, 1257–1265 (1998).
[10] T. L. Chenevert, S. Y. Emelianov, and A. R. Skovoroda, ''Elasticity reconstructive imaging using static displacement and strain estimations,'' in Proc. of the Int. Soc. of Magnetic Resonance in Medicine, 461.
[11] T. L. Chenevert, A. R. Skovoroda, M. O'Donnell, and S. Y. Emelianov, ''Elasticity reconstructive imaging by means of stimulated echo MRI,'' Magn. Reson. Med. **39**, 482–490 (1998).
[12] C. J. Lewa, ''Magnetic resonance imaging in the presence of mechanical waves,'' Spectrosc. Lett. **24**, 55–67 (1991).
[13] R. Muthupillai, P. J. Rossman, D. J. Lomas, J. F. Greenleaf, S. J. Riederer, and R. L. Ehman, ''Magnetic resonance imaging of transverse acoustic strain waves,'' Magn. Reson. Med. **36**, 266–274 (1996).
[14] R. Muthupillai, D. J. Lomas, P. J. Rossman, J. F. Greenleaf, A. Manduca, and R. L. Ehman, ''Magnetic resonance elastography by direct visualization of propagating acoutsic strain waves,'' Science **269**, 1854–1857 (1995).
[15] C. Sumi and K. Nakayama, ''A robust numerical solution to reconstruct a globally relative shear modulus distribution from strain measurements,'' IEEE Trans. Med. Imaging **17**, 419–428 (1998).
[16] K. R. Raghavan and A. E. Yagle, ''Forward and inverse problems in elasticity imaging of soft tissues,'' IEEE Trans. Nucl. Sci. **41**, 1639–1648 (1994).
[17] A. Manduca, R. Muthupillai, P. J. Rossman, J. F. Greenleaf, and R. L. Ehman, ''Image processing for magnetic resonance elastography,'' Proc. SPIE **2710**, 616–623 (1996).
[18] K. D. Paulsen and H. Jiang, ''Spatially varying optical property reconstruction using a finite element diffusing equation approximation,'' Med. Phys. **22**, 691–701 (1995).
[19] K. D. Paulsen and H. Jiang, ''An enhanced electrical impedence imaging algorithm for hyperthermia applications,'' Int. J. Hyperthermia **13**, 459–480 (1997).
[20] E. E. W. Van Houten, K. D. Paulsen, M. I. Miga, F. E. Kennedy, and J. B. Weaver, ''An overlapping subzone technique for MR based elastic property reconstruction,'' Magn. Reson. Med. **42**, 779–786 (1999).
[21] A. Manduca, V. Dutt, D. T. Borup, R. Muthupillai, R. L. Ehman, and J. F. Geenleaf, ''Reconstruction of elasticity and attenuation maps in shear wave imaging: An inverse approach,'' in *Lecture Notes in Computer Science—Medical Image Computing and Computer-Assisted Intervention '98*, edited by W. M. Wells, A. Colchester, and S. Delp (Springer-Verlag, Berlin, 1496), pp. 606–613.
[22] F. Kallel and M. Bertrand, ''Tissue elasticity reconstruction using linear perturbation method,'' IEEE Trans. Med. Imaging **15**, 299–313 (1996).
[23] D. W. Marquardt, ''An algorithm for least-squares estimation of nonlinear parameters,'' SIAM (Soc. Ind. Appl. Math.) J. Appl. Math. **11**, 431–441 (1963).
[24] P. C. Chou and N. J. Pagano, *Elasticity; Tensor, Dyadic and Engineering Approaches* (Dover, New York, 1967).